
Information Robust Dirichlet Networks for Predictive Uncertainty Estimation

Theodoros Tsiligkaridis

MIT Lincoln Laboratory, Lexington, MA 02421 USA

Abstract

Precise estimation of uncertainty in predictions for AI systems is a critical factor in ensuring trust and safety. Conventional neural networks tend to be overconfident as they do not account for uncertainty during training. In contrast to Bayesian neural networks that learn approximate distributions on weights to infer prediction confidence, we propose a novel method, Information Robust Dirichlet networks, that learns the Dirichlet distribution on prediction probabilities by minimizing the expected L_p norm of the prediction error and an information divergence loss that penalizes information flow towards incorrect classes, while simultaneously maximizing differential entropy of small adversarial perturbations to provide accurate uncertainty estimates. Properties of the new cost function are derived to indicate how improved uncertainty estimation is achieved. Experiments using real datasets show that our technique outperforms state-of-the-art neural networks, by a large margin, for estimating in-distribution and out-of-distribution uncertainty, and detecting adversarial examples.

2016), bioinformatics (Alipanahi et al., 2015), other aspects of deep learning are less well understood. Conventional neural networks (NNs) are overconfident in their predictions (Guo et al., 2017) and provide inaccurate predictive uncertainty (Louizos and Welling, 2017). Interpretability, robustness, and safety are becoming increasingly important as deep learning is being deployed across various industries including healthcare, autonomous driving and cybersecurity.

Uncertainty modeling in deep learning is a crucial aspect that has been the topic of various Bayesian neural network (BNN) research studies (Blundell et al., 2015; Kingma et al., 2015; Gal and Ghahramani, 2016; Molchanov et al., 2017). BNNs capture parameter uncertainty of the network by learning distributions on weights and estimate a posterior predictive distribution by approximate integration over these parameters. The non-linearities embedded in deep neural networks make the weight posterior intractable and several tractable approximations have been proposed and trained using variational inference (Blundell et al., 2015; Kingma et al., 2015; Molchanov et al., 2017; Gal and Ghahramani, 2016; Li and Gal, 2017), the Laplace approximation (MacKay, 1992; Ritter et al., 2018), expectation propagation (Hernandez-Lobato and Adams, 2015; Sun et al., 2017), and Hamiltonian Monte Carlo (Chen et al., 2014). The success of approximate BNN methods depends on how well the approximate weight distributions match their true counterparts, and their computational complexity is determined by the degree of approximation. Most BNNs take more effort to implement and are harder to train in comparison to conventional NNs. Furthermore, approximate integration over the parameter uncertainties increases the test time due to posterior sampling, and yields an approximate predictive distribution that is subject to bias, due to stochastic averaging. Thus, it is of interest to develop methods that provide good uncertainty estimates while reusing the training pipeline and maintaining scalability. To this end, a simple approach was proposed by (Lakshminarayanan et al., 2017) that combines NN ensembles with adversarial training to improve predictive uncertainty estimates in a non-Bayesian manner. It is

1 INTRODUCTION

Deep learning systems have achieved state-of-the-art performance in various domains (LeCun et al., 2015). The first successful applications of deep learning include large-scale object recognition (Krizhevsky et al., 2012) and machine translation (Sutskever et al., 2014; Wu et al., 2016). While further advances have achieved strong performance and often surpass human-level ability in computer vision (Geirhos et al., 2018; He et al., 2015; Ciresan et al., 2012), speech recognition (Xiong et al., 2017; Hinton et al., 2012), medicine (Wang et al.,

known that deterministic NNs are brittle to adversarial attacks (Goodfellow et al., 2014; Kurakin et al., 2017) and various defenses have been proposed to increase accuracy for low levels of noise (Madry et al., 2018). Recently, a study (Lee et al., 2018) used generative adversarial networks to generate boundary samples and trained the classifier to be uncertain on those as a means to improve detection of out-of-distribution samples. While adversarial defense has been explored, the idea of maximizing uncertainty on low-noise adversarial examples to improve predictive uncertainty estimates has not been investigated to the best of our knowledge.

Recently, in (Sensoy et al., 2018; Malinin and Gales, 2019) the Dirichlet distribution was used to model distributions of class compositions and its parameters were learned by training deterministic neural networks. This approach for Bayesian classification yields closed-form predictive distributions and outperforms BNNs in uncertainty quantification for out-of-distribution and adversarial queries. However, uncertainty estimation performance for in-distribution queries was not studied, and out-of-distribution and adversarial queries performance can be significantly improved.

In this paper, we propose Information Robust Dirichlet networks that deliver more accurate predictive uncertainty than other state-of-the-art methods. Our method modifies the output layer of neural networks and the training loss, therefore maintaining computational efficiency and ease of implementation. The contributions are as follows. First, a new training loss based on minimizing the expected L_p norm of the prediction error is proposed under which the prediction probabilities follow a Dirichlet distribution. A closed-form approximation to this loss is derived, under which a deterministic neural network is trained to infer the parameters of a Dirichlet distribution, effectively teaching neural networks to learn distributions over class probability vectors. Second, an information divergence is used to regularize the estimated Dirichlet distribution and a maximum entropy penalty on adversarial examples is used to maximize uncertainty near the edge of the data distribution. Third, an analysis is provided that shows how properties of the new loss improve uncertainty estimation. Finally, we demonstrate on real datasets that our technique obtains unmatched success in terms of uncertainty estimation for correct and incorrect predictions, detection of out-of-distribution queries and adversarial attacks.

2 PITFALLS OF CONVENTIONAL SOFTMAX

The conventional approach for the classification layer includes the softmax operator which takes continuous-

valued activations of the output layer and converts them into probabilities. Typically the cross-entropy loss is used for training which does not account for uncertainty. As noted in Gal and Ghahramani (2016); Louizos and Welling (2017); Sensoy et al. (2018), the exponentiation involved to form a point estimate of the class probabilities tends to inflate them deteriorating uncertainty estimates derived from the softmax probabilities. As a result, uncertainty estimation suffers due to the parametrization and the fact that the training loss does not account for uncertainty. This is illustrated in Fig. 1 in which an image of a digit 6 is correctly classified initially, but as it rotates the softmax output incorrectly classifies it with high probability as an 8.¹ In contrast, our approach yields a near-uniform distribution during the rotation stage and thus provides a reasonable uncertainty estimate using the entropy of the predictive distribution.

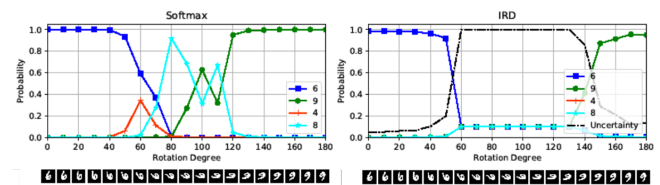


Figure 1: Classification of rotated digit 6 spanning a 180-degree rotation for standard neural network with softmax output (left) and our proposed approach (right).

3 LEARNING DISTRIBUTIONS ON THE PROBABILITY SIMPLEX

3.1 Dirichlet Distribution

Outputs of standard neural networks for classification tasks are probability vectors over classes. The basis of our approach lies in modeling the distribution of such probability vectors for each example using the Dirichlet distribution (Mauldon, 1959; Mosimann, 1962). Given the probability simplex as $\mathcal{S} = \{(p_1, \dots, p_K) : p_i \geq 0, \sum_i p_i = 1\}$, the Dirichlet distribution is a probability density function on vectors $\mathbf{p} \in \mathcal{S}$ given by

$$f_{\alpha}(\mathbf{p}) = \frac{1}{B(\alpha)} \prod_{j=1}^K p_j^{\alpha_j - 1}$$

where $B(\alpha) = \prod_{j=1}^K \Gamma(\alpha_j) / \Gamma(\alpha_0)$ is the multivariate Beta function. It is characterized by K parameters $\alpha = (\alpha_1, \dots, \alpha_K)$ here assumed to be larger than unity.

¹We remark that the networks are trained on MNIST without rotated data augmentations.

² In the special case of the all-ones α vector, the distribution becomes uniform over the probability simplex. The mean of the proportions is given by $\hat{p}_j = \alpha_j / \alpha_0$, where $\alpha_0 = \sum_j \alpha_j$ is the Dirichlet strength. The Dirichlet distribution is conjugate to the multinomial distribution, with posterior parameters updated as $\alpha'_j = \alpha_j + y_j$ for a multinomial sample $\mathbf{y} = (y_1, \dots, y_K)$. For a single sample, $y_j = I_{\{j=c\}}$, where c is the index of the correct class.

The marginal distributions of the Dirichlet distribution are Beta random variables, specifically, $p_j \sim \text{Beta}(\alpha_j, \alpha_0 - \alpha_j)$ with support on $[0, 1]$. The q -th moment of the Beta distribution $\text{Beta}(\alpha', \beta')$ is given by

$$\mathbb{E}[p^q] = \int_0^1 p^q \frac{p^{\alpha'-1}(1-p)^{\beta'-1}}{B_u(\alpha', \beta')} dp = \frac{B_u(\alpha' + q, \beta')}{B_u(\alpha', \beta')} \quad (1)$$

where $B_u(\alpha', \beta') = \Gamma(\alpha')\Gamma(\beta')/\Gamma(\alpha' + \beta')$ is the univariate Beta function.

3.2 Classification Loss

Consider given data $\{\mathbf{x}_i\}$ and associated labels $\{\mathbf{y}_i\}$ drawn from a set of K classes. We model the class probability vectors for sample i given by \mathbf{p}_i as random vectors drawn from a Dirichlet distribution conditioned on the input \mathbf{x}_i . A neural network with input \mathbf{x}_i is trained to learn this Dirichlet distribution, $f_{\alpha_i}(\mathbf{p}_i)$, with output α_i . While the layers of the Dirichlet neural network can be similar to classical NNs, the softmax classification layer is replaced by a softplus activation layer that outputs non-negative continuous values, e.g., $g_\alpha(\mathbf{x}_i; w) \in \mathbb{R}_+^K$ where w are the network parameters, from which we obtain $\alpha_i = g_\alpha(\mathbf{x}_i; w) + 1$.

Given one-hot encoded labels \mathbf{y}_i of examples \mathbf{x}_i with correct class c_i , the Bayes risk of the L_p prediction error for $p \geq 1$ is approximated using Jensen's inequality as

$$\begin{aligned} \mathbb{E}\|\mathbf{y}_i - \mathbf{p}_i\|_p &\leq \left(\mathbb{E}[\|\mathbf{y}_i - \mathbf{p}_i\|_p^p] \right)^{1/p} \\ &= \left(\mathbb{E}[(1 - p_{i,c_i})^p] + \sum_{j \neq c_i} \mathbb{E}[p_{i,j}^p] \right)^{1/p} =: \mathcal{F}_i(w) \end{aligned}$$

The max-norm can be approximated by using a large p . To calculate each term, we note $1 - p_{i,c_i}$ has a distribution $\text{Beta}(\alpha_{i,0} - \alpha_{i,c_i}, \alpha_{i,c_i})$ due to mirror symmetry, and $p_{i,j}$ has distribution $\text{Beta}(\alpha_{i,j}, \alpha_{i,0} - \alpha_{i,j})$. Using

²The reason for this constraint is that the Dirichlet distribution becomes inverted for $\alpha_j < 1$ concentrating in the corners of the simplex and along its boundaries.

the moment expression (1) for Beta random variables:

$$\begin{aligned} \mathcal{F}_i(w) &= \left(\frac{B_u(\alpha_{i,0} - \alpha_{i,c_i} + p, \alpha_{i,c_i})}{B_u(\alpha_{i,0} - \alpha_{i,c_i}, \alpha_{i,c_i})} \right. \\ &\quad \left. + \sum_{j \neq c_i} \frac{B_u(\alpha_{i,j} + p, \alpha_{i,0} - \alpha_{i,j})}{B_u(\alpha_{i,j}, \alpha_{i,0} - \alpha_{i,j})} \right)^{\frac{1}{p}} \\ &= \left(\frac{\Gamma(\alpha_0)}{\Gamma(\alpha_0 + p)} \right)^{\frac{1}{p}} \left(\frac{\Gamma\left(\sum_{k \neq c} \alpha_k + p\right)}{\Gamma\left(\sum_{k \neq c} \alpha_k\right)} + \sum_{k \neq c} \frac{\Gamma(\alpha_k + p)}{\Gamma(\alpha_k)} \right)^{\frac{1}{p}} \end{aligned}$$

The following theorem shows that the loss function \mathcal{F}_i has the correct behavior as the information flow increases towards the correct class which is consistent when an image sample of that class is observed in a Bayesian Dirichlet experiment and hyperparameters are incremented (see Sec. 3.1).

Theorem 1. *For a given sample \mathbf{x}_i with correct label c , the loss function \mathcal{F}_i is strictly convex and decreasing in α_c increases (and increases when α_c decreases).*

Theorem 1 shows that our objective function encourages the learned distribution of probability vectors to concentrate towards the correct class. While increasing information flow towards the correct class reduces the loss, it is also important for the loss to capture elements of incorrect classes. It is expected that increasing information flow towards incorrect classes increases uncertainty. The next result shows that through our loss function the model avoids assigning high concentration parameters to incorrect classes as the model cannot explain observations that are assigned incorrect outcomes.

Theorem 2. *For a given sample \mathbf{x}_i with correct label c , the loss function \mathcal{F}_i is increasing in α_j for any $j \neq c$ as α_j grows.*

Theorem 2 implies that our loss function leads the model to push the distribution of class probability vectors away from incorrect classes. The proofs are included in the supplementary material.

3.3 Information Divergence Regularization Loss

The classification loss can discover interesting patterns in the data to achieve high classification accuracy. However, the network may learn that certain patterns lead to strong information flow towards incorrect classes, e.g., circular pattern of digit 6 might contribute to a large α associated with digit 8.

We regularize the Dirichlet distribution f_{α} to concentrate away from incorrect classes. Given the auxiliary vector $\alpha'_i = (1 - \mathbf{y}_i) + \mathbf{y}_i \odot \alpha_i$, we minimize the Rényi information divergence (Rényi, 1961; Erven and Harremo, 2014) of the Dirichlet distribution f_{α} from $f_{\alpha'}$:

$$\begin{aligned} D_u^R(f_{\alpha} \parallel f_{\alpha'}) &= \frac{1}{u-1} \log \int_S f_{\alpha}(\mathbf{p})^u f_{\alpha'}(\mathbf{p})^{1-u} d\mathbf{p} \\ &= \frac{1}{u-1} \log \left[\frac{B(u\alpha + (1-u)\alpha')}{B(\alpha)^u B(\alpha')^{1-u}} \right] \\ &= \log \left[\frac{B(\alpha')}{B(\alpha)} \right] + \frac{1}{u-1} \log \left[\frac{B(u\alpha + (1-u)\alpha')}{B(\alpha)} \right] \end{aligned} \quad (2)$$

The order $u > 0$ controls the influence of the likelihood ratio $f_{\alpha}/f_{\alpha'}$ on the divergence. This divergence is minimized if and only if $\alpha_i = \alpha'_i$, in other words when $\alpha_{ij} = 1$ for $j \neq c_i$. The extended order $u = 1$ yields the Kullback-Leibler divergence.

The next theorem presents a local approximation of the divergence (2) in terms of Fisher information matrix $J(\alpha) = \mathbb{E}[\nabla \log f_{\alpha}(\mathbf{p}) \nabla \log f_{\alpha}(\mathbf{p})^T] = -\mathbb{E}[\nabla^2 \log f_{\alpha}(\mathbf{p})]$.

Theorem 3. As $\|\alpha - \alpha'\|_2^2 = \sum_{j \neq c} (\alpha_j - 1)^2 \rightarrow 0$, the Rényi divergence can be locally approximated as:

$$\begin{aligned} D_u^R(f_{\alpha} \parallel f_{\alpha'}) &\cong \frac{u}{2} (\alpha - \alpha')^T J(\alpha) (\alpha - \alpha') \\ &= \frac{u}{2} \left[\sum_{i \neq c} (\alpha_i - 1)^2 \psi^{(1)}(\alpha_i) - \left(\sum_{i \neq c} (\alpha_i - 1) \right)^2 \psi^{(1)}(\alpha_0) \right] \end{aligned}$$

where $\psi^{(1)}(z) = \frac{d}{dz} \psi(z)$ is the polygamma function of order 1.

Theorem 3 shows that as $\{\alpha_j\}_{j \neq c} \rightarrow 1$ during the training process, the regularization term becomes proportional to the order u that controls the local curvature of the divergence function.

Furthermore, the asymptotic approximation has an interesting behavior for various confidence levels α_c . Since the polygamma function is monotonically decreasing, it satisfies $\psi^{(1)}(\alpha_c + \sum_{i \neq c} \alpha_i) > \psi^{(1)}(\alpha'_c + \sum_{i \neq c} \alpha_i)$ for $\alpha_c < \alpha'_c$. Theorem 3 implies that during training, examples that exhibit larger confidence for the correct class c have a higher Rényi divergence associated with them compared to ones with a lower confidence α_c . This is numerically illustrated in Fig. 2 as a function of α_i for some $i \neq c$, when all concentration parameters are held fixed close to 1 and α_c has a low or high value. This implies that the model tends to learn to yield sharper Dirichlet distributions when the correct class confidence is higher since the Rényi divergence is minimized by concentrating away from incorrect classes through $\{\alpha_j\}_{j \neq c} \rightarrow 1$.

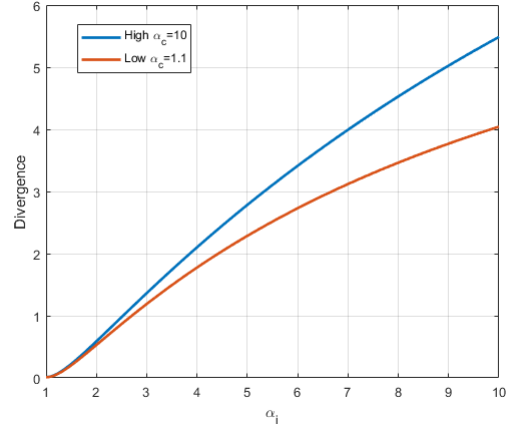


Figure 2: Rényi divergence illustration as $\alpha_i, i \neq c$ varies for the regime $\{\alpha_j\}_{j \neq c} \rightarrow 1$ with two different values for the correct class concentration parameter α_c . Here, $u = 2$ and $K = 10$.

3.4 Maximum Adversarial Entropy Regularization Loss

To further improve the network robustness, we first generate low-noise adversarial examples using the fast gradient sign method (FGSM) (Goodfellow et al., 2014),

$$\mathbf{x}_{adv} = \mathbf{x} + \epsilon \cdot \text{sgn}(\nabla_{\mathbf{x}} \mathcal{F}(\mathbf{x}, y, w)).$$

Then the Dirichlet network generates α_{adv} that parametrize a distribution on the simplex $f(\mathbf{p}|\mathbf{x}_{adv}, w) = f_{\alpha_{adv}}(\mathbf{p})$, and we maximize the differential entropy of this Dirichlet distribution:

$$\begin{aligned} \mathcal{H}(f_{\alpha_{adv}}(\mathbf{p})) &= - \int_S f_{\alpha_{adv}}(\mathbf{p}) \log f_{\alpha_{adv}}(\mathbf{p}) d\mathbf{p} \\ &= \log B(\alpha_{adv}) + (\alpha_{0,adv} - K) \psi(\alpha_{0,adv}) \\ &\quad - \sum_{j=1}^K (\alpha_{j,adv} - 1) \psi(\alpha_{j,adv}) \end{aligned}$$

This differential entropy captures distributional uncertainty and is maximized when all probability vectors have the same likelihood (pushing α_{adv} towards the all-ones vector). This penalty has the effect of robustifying the predictive Dirichlet distributions inferred by the network so that small adversarial perturbations of the inputs yield high distributional uncertainty. In our experiments we find that this improves the out-of-distribution uncertainty estimation performance as well.

The total loss is $\mathcal{G}_i = \mathcal{F}_i + \lambda D_u^R(f_{\alpha_i} \parallel f_{\alpha'_i}) - \gamma \mathcal{H}(f_{\alpha_{i,adv}})$ where λ, γ are nonnegative parameters controlling the tradeoff between minimizing the approximate Bayes risk and the information regularization penalties. The total loss is summed over a batch of training samples $\mathcal{G}(w) = \sum_{i=1}^N \mathcal{G}_i(w)$. Training is performed using

minibatches and the adversarial FGSM examples are generated for every minibatch as training progresses with λ, γ increasing using an annealing schedule, e.g., $\lambda_t = \lambda(1 - e^{-0.05t})$, $\gamma_t = \gamma \min(1, t/40)$.

3.5 Uncertainty Metrics

Dirichlet networks generate $\alpha = g_\alpha(\mathbf{x}^*; w) + 1$ that correspond to a Dirichlet distribution on the simplex $f(\mathbf{p}|\mathbf{x}^*, w) = f_\alpha(\mathbf{p})$. The predictive distribution is given by

$$P(y = j|\mathbf{x}^*; w) = \mathbb{E}_{f_\alpha(\mathbf{p})}[P(y = j|\mathbf{p})] = \frac{\alpha_j}{\alpha_0}$$

Predictive entropy measures total uncertainty and can be decomposed into knowledge uncertainty (arises due to model’s difficulty in understanding inputs) and data uncertainty (arises due to class-overlap and noise) (Malinin and Gales, 2019). This uncertainty metric is given by:

$$H(\mathbb{E}_{f_\alpha(\mathbf{p})}[P(y|\mathbf{p})]) = - \sum_j \frac{\alpha_j}{\alpha_0} \log \frac{\alpha_j}{\alpha_0}$$

The mutual information between the labels y and the class probability vector \mathbf{p} , $I(y, \mathbf{p}|\mathbf{x}^*; w)$, captures knowledge uncertainty, and can be calculated by subtracting the expected data uncertainty from the total uncertainty:

$$\begin{aligned} I(y, \mathbf{p}|\mathbf{x}^*; w) &= H(\mathbb{E}_{f_\alpha(\mathbf{p})}[P(y|\mathbf{p})]) - \mathbb{E}_{f_\alpha(\mathbf{p})}[H(P(y|\mathbf{p}))] \\ &= - \sum_j \frac{\alpha_j}{\alpha_0} \left(\log \frac{\alpha_j}{\alpha_0} - \psi(\alpha_j + 1) + \psi(\alpha_0 + 1) \right) \end{aligned}$$

This metric is useful when measuring uncertainty for out-of-distribution or adversarial examples, and a variation of it was used in the context of active learning (Houlsby et al., 2011).

4 EXPERIMENTAL RESULTS

All experiments are implemented in Tensorflow (Abadi et al., 2016) and the Adam (Kingma and Ba, 2015) optimizer was used for training.

4.1 MNIST Dataset

We follow the same experimental setup as in (Louizos and Welling, 2017) and (Sensoy et al., 2018). The LeNet CNN architecture with 20 and 50 filters of size 5×5 is used for the MNIST dataset (LeCun et al.) with 500 hidden units at the dense layer. The training set contains 60,000 digits and the testing set contains 10,000. Comparisons are made with the following methods: (a) L2 corresponds to deterministic neural network with softmax output and weight decay, (b)

Table 1: MNIST Dataset: Test accuracy (%), median % max-entropy for correct and misclassified examples for various deep learning methods

Method	Accuracy	Median %Max-Entropy Correct	Median %Max-Entropy Misclassified
L2	99.4	-	-
Dropout	99.5	-	-
Deep Ensemble	99.3	-	-
FFG	99.1	-	-
FFLU	99.1	-	-
MNFG	99.3	-	-
PN	99.3	19.5	56.7
EDL	99.2	24.9	99.6
IRD	98.2	6.4	100.0

Dropout is the uncertainty estimation method of (Gal and Ghahramani, 2016), (c) Deep Ensemble is the non-Bayesian approach of (Lakshminarayanan et al., 2017), (d) FFG is the BNN used in (Blundell et al., 2015), (e) FFLU is the BNN used in (Kingma et al., 2015) with the additive parameterization (Molchanov et al., 2017), (f) MNFG is the multiplicative normalizing flow VI inference method in (Louizos and Welling, 2017), (g) PN is the reverse KL divergence-based prior network method of (Malinin and Gales, 2019), (h) EDL is the evidential approach of (Sensoy et al., 2018) and (i) IRD is our proposed technique. In our implementation of PN and IRD, FGSM adversarial examples were generated using $\epsilon = 0.1$ noise. Hyperparameter values $u = 2.0, \lambda = 0.5, \gamma = 0.1$ were used to generate these results with $p = 15$. Table 1 shows the test accuracy on MNIST for these methods; IRD is shown to be competitive assigning low uncertainty to correct predictions and high uncertainty to misclassifications.

Fig. 3 shows the distribution of entropies of predictive distributions for correct and misclassified examples across competing methods. The overconfidence of softmax NNs is evident since both correct and wrong entropy distributions are concentrated on lower uncertainties. The Dirichlet-based methods, EDL and PN, are better calibrated offering a good balance between correct and misclassified entropies. IRD offers a drastic improvement over all methods with 90% of the misclassified samples falling within 95% of the max-entropy ($\log 10 \approx 2.3$), as opposed to 58% and 5% of the misclassified samples of the PN and EDL methods respectively.

IRD is tested on notMNIST (Bulatov, 2011) which contains only letters serving as out-of-distribution data. The uncertainty is expected to be high for all such

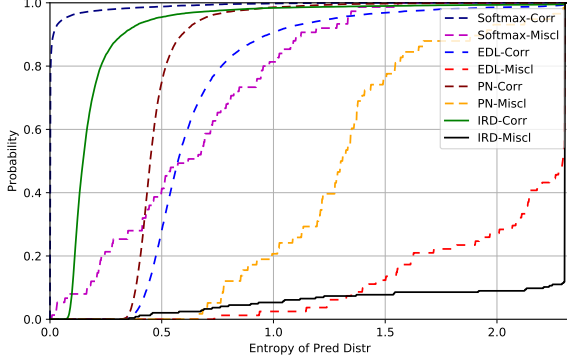


Figure 3: Empirical CDF of predictive distribution entropy on MNIST dataset.

images as letters do not fit into any digit category. Fig. 4 shows the empirical CDF of the predictive entropy for all models. CDF curves close to the bottom right are more desirable as higher entropy is desired for all predictions. IRD is much more tightly concentrated towards higher entropy values with an impressive 96% of letter images having entropy larger than 95% of the max-entropy, while EDL and PN have 61% and 63% approximately.

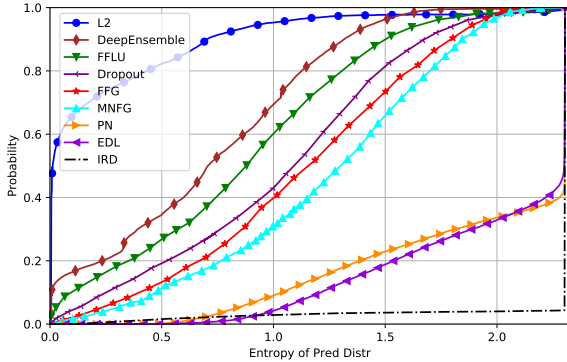


Figure 4: Empirical CDF of predictive distribution entropy on notMNIST dataset.

Fig. 5 shows the adversarial performance when each model is evaluated using adversarial examples generated with the Fast Gradient Sign method (FGSM) (Goodfellow et al., 2014) for different noise values ϵ , i.e., $\mathbf{x}_{adv} = \mathbf{x} + \epsilon \text{sgn}(\nabla_{\mathbf{x}} \mathcal{F}(\mathbf{x}, y, w))$. We observe that IRD achieves higher entropy on adversarial examples as ϵ increases. Dropout outperforms other BNN methods at the expense of overconfident predictions. While PN asymptotically achieves very high uncertainty as well to the same level as IRD, we remark that IRD achieves a lower average predictive entropy for $\epsilon = 0$ due to the higher confidence of correct predictions and assigns a large entropy to misclassified samples as Fig. 3 also supports.

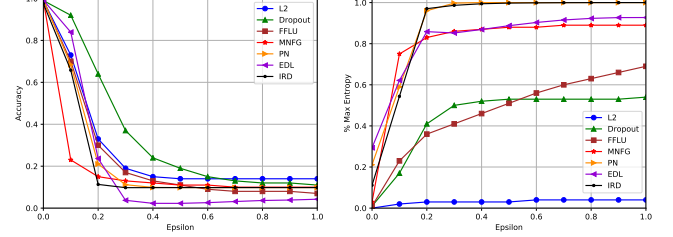


Figure 5: Test accuracy (left) and predictive entropy (right) for FGSM adversarial examples as a function of adversarial noise ϵ on MNIST dataset.

Fig. 6 shows the adversarial performance of the Dirichlet-based methods (the most competitive ones) on examples generated with the projected gradient descent (PGD) method (Kurakin et al., 2017) for different noise levels ϵ , i.e., $\mathbf{x}_{adv}^{t+1} = \Pi_{\mathbf{x}+\epsilon\ell_\infty}(\mathbf{x}_{adv}^t + \alpha \text{sgn}(\nabla_{\mathbf{x}} \mathcal{F}(\mathbf{x}_{adv}^t, y, w)))$ with $\mathbf{x}_{adv}^0 = \mathbf{x}$. Here, $\Pi_{\mathbf{x}+\epsilon\ell_\infty}(\cdot)$ is the projection onto the ℓ_∞ ball of size ϵ centered at \mathbf{x} . This multi-step variant of FGSM uses a small step size $\alpha = 0.01$ over $T = 40$ steps. We observe that IRD achieves the highest uncertainty on PGD adversarial examples as the noise level increases while PN asymptotically achieves a mid-range uncertainty, EDL is inconsistent and Softmax NNs cannot reliably detect these stronger attacks. We further remark that IRD has lower predictive entropy for $\epsilon = 0$ due to the higher confidence of correct predictions as Fig. 3 also shows.

4.2 PhysioNet ECG Dataset

The PhysioNet17 challenge dataset (Clifford et al., 2017) contains 5,707 electrocardiogram (ECG) signals of length 9,000 sampled at 300 samples/sec. The task we consider is binary classification of short single-lead ECG recordings into a normal sinus rhythm or atrial fibrillation (Afib). Atrial fibrillation is the most common sustained cardiac arrhythmia occurring when the heart’s upper chambers beats out of synchronization with the lower chambers, and is hard to detect due to its episodic presence. The raw ECG signals were bandpass filtered for baseline wander removal, and then normalized to zero mean and unit variance over the 30s duration.

The CNN architecture consists of six 1D Conv layers with stride-2 max-pooling, with 8, 16, 32, 64, 128, 128 filters of sizes 9, 9, 7, 7, 5, 5 respectively, followed by a filter-wise sum-pooling layer, 100 hidden units with dropout and a binary classification layer. About 13% of the recordings correspond to Afib, and oversampling was used to account for class imbalance. A train/test split of 90%/10% was used. As EDL and PN were shown to be most competitive with our

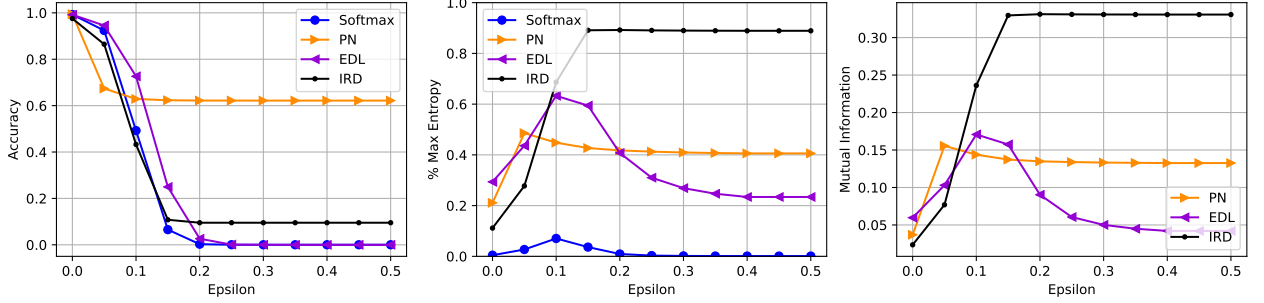


Figure 6: Test accuracy (left), predictive entropy (middle), and mutual information (right) for PGD adversarial examples as a function of adversarial noise ϵ on MNIST dataset.

Table 2: PhysioNet ECG Dataset: Test accuracy (%), median % max-entropy for correct and misclassified examples for various deep learning methods

Method	Accuracy	Median %Max-Entropy Correct	Median %Max-Entropy Misclassified
L2	94	1.7	81.4
Dropout	94	4.2	70.4
PN	96	15.1	65.0
EDL	95	23.4	59.5
IRD	95	10.2	100.0

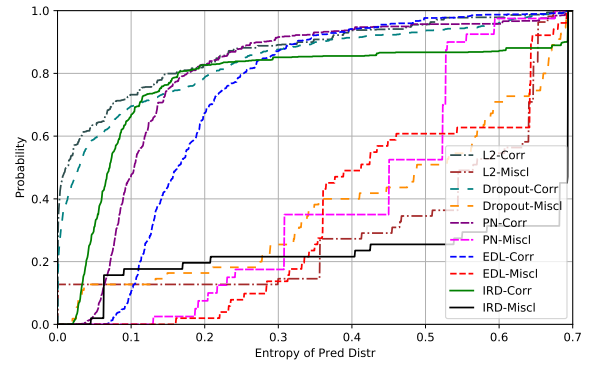


Figure 7: Empirical CDF of predictive entropy on correct and misclassified ECG signals for various deep learning methods.

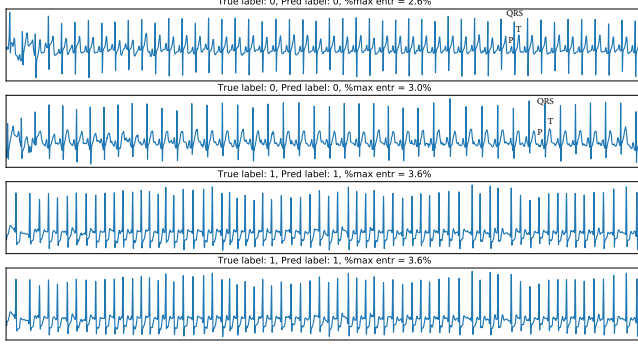
method based on the benchmark image dataset shown above, we compare IRD with the L2, Dropout, PN and EDL methods. The hyperparameters used were $u = 0.95$, $\lambda = 2.3$, $\gamma = 0.07$, $\epsilon = 0.02$ with $p = 15$.

The accuracies of all methods are shown in Table 2 and IRD achieves a high prediction accuracy on par with other methods. Fig. 7 shows the cumulative density function of the predictive entropy for correct and misclassified examples. The median entropy normalized by the maximum entropy is shown in the last two columns of Table 2, which reflects that IRD assigns very low uncertainty for correct classifications and large uncertainty to misclassifications. The tail of the entropy distribution of misclassified samples shows that IRD assigns entropy values larger than 90% of the max-entropy to 69% of the misclassified samples while L2, Dropout, PN and EDL methods assign that to only 44%, 27%, 3% and 37% of their misclassified examples respectively.

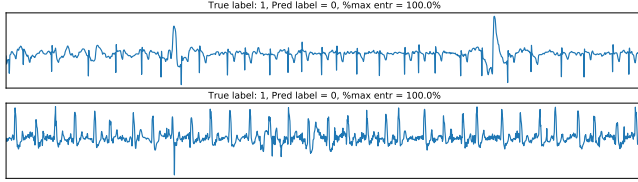
Fig. 8 shows correct and misclassified ECG signals from the test set; the top plots show correctly classified normal rhythms (top two) and AFib (next two) signals with low prediction entropy, and the bottom two plots show incorrectly classified AFib signals characterized by high prediction entropy. It is evident that the algo-

rithm correctly forms high-confidence opinions about signals that exhibit strong characteristics of normal heartbeat (e.g., regular occurrence with identifiable P wave, QRS complex and T wave) and AFib (e.g., irregular spacing of pulses with often a lack of a P wave). Visual inspection of the high-entropy misclassified signals show that although local peaks tend to be irregular hinting at AFib, but there is too much noise in the intermediate waves and transient irregularity to reliably classify them.

To test detection of out-of-distribution signals, we constructed a modified dataset from the test set by adding sparse random noise (zero-mean Gaussian with $\sigma = 5$ at 5% of total time locations uniformly at random) followed by temporally smoothing the whole waveform with a 1D Gaussian filter of $\sigma = 15$. Fig. 9 contains several anomalous generated waveforms. Empirical CDFs of predictive entropy and mutual information are shown in Fig. 10, in which IRD outperforms other methods by a large margin. Specifically, IRD assigns a predictive entropy of 90% max-entropy or higher to 81% of the anomalous signals as opposed to 17%, 27%, 6%, 20% for L2, Dropout, PN and EDL methods respectively.



(a)



(b)

Figure 8: (a) Correctly classified ECG signals with low uncertainty. (b) Misclassified ECG signals with high uncertainty.

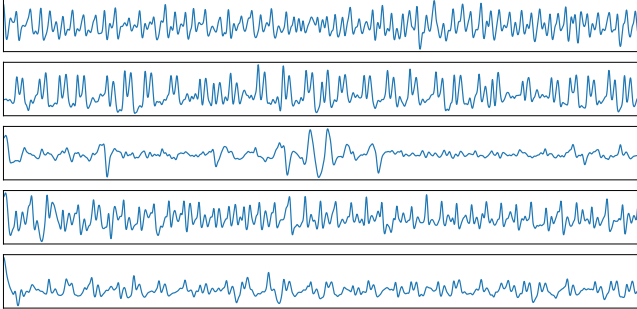


Figure 9: Sample out-of-distribution signals for PhysioNet ECG dataset.

5 CONCLUSION

In this work we presented a new method for training Dirichlet neural networks that are aware of the uncertainty associated with predictions. Our training objective that fits predictive distributions to data consisted of three elements; a calibration loss that minimizes the expected L_p norm of the prediction error, an information divergence loss that penalizes information flow towards incorrect classes, and a maximum entropy loss that maximizes uncertainty for small adversarial perturbations. We derived closed-form expressions for our training loss and desirable properties on how improved uncertainty estimation is achieved. Experimental results were shown on an image classification task and a ECG-based heart condition diagnosis task, highlighting

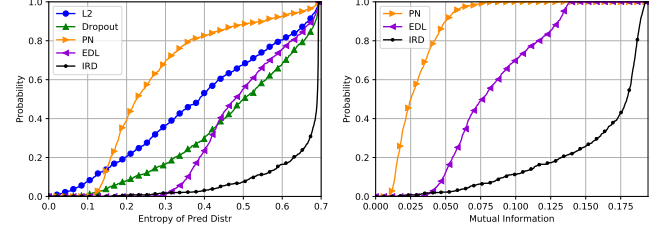


Figure 10: Empirical CDF of predictive entropy and mutual information on out-of-distribution signals for various deep learning methods.

the unmatched improvements in predictive uncertainty estimation made by our method over conventional softmax neural networks, Bayesian neural networks, and other recent Dirichlet networks trained with different criteria. Furthermore, due to the explicit modeling of the categorical distributions over classes, our approach does not require ensembling multiple predictions or performing multiple evaluations of the network at inference time (e.g., as BNNs do approximate integration over the parameter uncertainties to obtain approximate predictive distributions) to arrive at predictive distributions and compute uncertainty metrics.

Acknowledgements

DISTRIBUTION STATEMENT A. Approved for public release. Distribution is unlimited. This material is based upon work supported by the Under Secretary of Defense for Research and Engineering under Air Force Contract No. FA8702-15-D-0001. Any opinions, findings, conclusions or recommendations expressed in this material are those of the author(s) and do not necessarily reflect the views of the Under Secretary of Defense for Research and Engineering.

Appendix

We make use of the following lemmas in the proofs.

Lemma 1. *Consider the digamma function ψ . Assuming $x_1 > x_2 > 1$ and $p > 0$, the following inequality strictly holds:*

$$0 < \psi(x_1 + p) - \psi(x_2 + p) < \psi(x_1) - \psi(x_2)$$

Furthermore, we have $\lim_{x \rightarrow \infty} \psi(x + p) - \psi(x) = 0$.

Proof. Since $x_1 > x_2 > 1$, we can write $x_1 = s_1 + 1$ and $x_2 = s_2 + 1$ for some $s_1 > s_2$. Upon substitution of the Gauss integral representation $\psi(z + 1) = -\gamma + \int_0^1 \left(\frac{1-t^z}{1-t} \right) dt$ (here γ is the Euler-Mascheroni constant), we have:

$$\psi(x_1) - \psi(x_2) = \int_0^1 \left(\frac{t^{s_2} - t^{s_1}}{1-t} \right) dt$$

which is strictly positive since the integrand is positive for $t \in (0, 1)$. Using the integral representation again, the inequality $\psi(x_1 + p) - \psi(x_2 + p) < \psi(x_1) - \psi(x_2)$ is equivalent to:

$$\int_0^1 \left(\frac{(1-t^p)(t^{s_2} - t^{s_1})}{1-t} \right) dt > 0$$

which holds since the integrand is positive due to $t^p < 1$ and $t^{s_1} < t^{s_2}$. The limit of $\psi(x+p) - \psi(x)$ follows from the asymptotic expansion $\psi(x) = \log(x) - \frac{1}{2x} + O\left(\frac{1}{x^2}\right)$, which yields $\psi(x+p) - \psi(x) \sim \log(1+p/x) - \frac{1}{2(x+p)} + \frac{1}{2x} \rightarrow 0$ as $x \rightarrow \infty$. This concludes the proof. \square

Lemma 2. Consider the polygamma function of order 1 $\psi^{(1)}(z) = \frac{d}{dz}\psi(z)$. Assuming $x_1 > x_2 > 1$ and $p > 0$, the following inequality strictly holds:

$$\psi^{(1)}(x_1) - \psi^{(1)}(x_2) < \psi^{(1)}(x_1 + p) - \psi^{(1)}(x_2 + p) < 0$$

Proof. Proceeding similarly as in the Proof of Lemma 1, we write $x_1 = s_1 + 1$ and $x_2 = s_2 + 1$ for some $s_1 > s_2$. Upon substitution of the integral representation $\psi^{(1)}(z+1) = \int_0^1 \left(\frac{t^z}{1-t} \ln\left(\frac{1}{t}\right) \right) dt$, we have:

$$\psi^{(1)}(x_1) - \psi^{(1)}(x_2) = \int_0^1 \left(\frac{t^{s_1} - t^{s_2}}{1-t} \ln\left(\frac{1}{t}\right) \right) dt$$

which is strictly negative since the integrand is negative for $t \in (0, 1)$. Using the integral representation again, the inequality $\psi^{(1)}(x_1) - \psi^{(1)}(x_2) < \psi^{(1)}(x_1 + p) - \psi^{(1)}(x_2 + p)$ is equivalent to:

$$\int_0^1 \left(\frac{(1-t^p)(t^{s_1} - t^{s_2})}{1-t} \ln\left(\frac{1}{t}\right) \right) dt < 0$$

which holds true since $\ln(1/t) > 0$ for $t \in (0, 1)$. This concludes the proof. \square

Proof of Theorem 1

Proof. Taking the logarithm of \mathcal{F}_i , we have:

$$\begin{aligned} \log \mathcal{F}_i &= \frac{1}{p} \log \left(\frac{\Gamma(\alpha_0)}{\Gamma(\alpha_0 + p)} \right) \\ &+ \frac{1}{p} \log \left(\frac{\Gamma(\sum_{k \neq c} \alpha_k + p)}{\Gamma(\sum_{k \neq c} \alpha_k)} + \sum_{j \neq c} \frac{\Gamma(\alpha_j + p)}{\Gamma(\alpha_j)} \right) \end{aligned}$$

where the second term is independent of α_c . Letting the first term be denoted as $g(\alpha_c) := \frac{1}{p} \log \left(\frac{\Gamma(\alpha_0)}{\Gamma(\alpha_0 + p)} \right)$, it suffices to show $f(\alpha_c) := \exp(g(\alpha_c))$ is strictly convex and decreasing in α_c .

Differentiating $g(\alpha_c)$ twice we obtain:

$$\begin{aligned} g'(\alpha_c) &= \frac{1}{p} (\psi(\alpha_0) - \psi(\alpha_0 + p)) \\ g''(\alpha_c) &= \frac{1}{p} (\psi^{(1)}(\alpha_0) - \psi^{(1)}(\alpha_0 + p)) \end{aligned}$$

Lemmas 1 and 2 then yield that $g'(\alpha_c) < 0$ and $g''(\alpha_c) > 0$ respectively. Differentiating $f(\alpha_c)$ twice, we have:

$$f'(\alpha_c) = e^{g(\alpha_c)} g'(\alpha_c) \quad (3)$$

$$f''(\alpha_c) = e^{g(\alpha_c)} (g''(\alpha_c) + (g'(\alpha_c))^2) \quad (4)$$

Using the inequalities above and the positivity of $e^{g(\alpha_c)}$, it follows that $f'(\alpha_c) < 0$ and $f''(\alpha_c) > 0$. Thus, $f(\alpha_c)$ is a strictly convex decreasing function in α_c . This concludes the proof. \square

Proof of Theorem 2

Proof. Consider a concentration parameter α_j corresponding to an incorrect class, i.e., $j \neq c$. Define the ratio of Gamma functions as:

$$\mu(\alpha) \stackrel{\text{def}}{=} \frac{\Gamma(\alpha + p)}{\Gamma(\alpha)}$$

This function is positive, increasing and convex with derivative given by:

$$\begin{aligned} \mu'(\alpha) &= -\frac{\Gamma(\alpha + p)\Gamma'(\alpha)}{\Gamma(\alpha)^2} + \frac{\Gamma'(\alpha + p)}{\Gamma(\alpha)} \\ &= -\frac{\Gamma(\alpha + p)\psi(\alpha)}{\Gamma(\alpha)} + \frac{\Gamma(\alpha + p)\psi(\alpha + p)}{\Gamma(\alpha)} \\ &= \mu(\alpha) (\psi(\alpha + p) - \psi(\alpha)) \\ &= \mu(\alpha) \nu(\alpha) \end{aligned} \quad (5)$$

where we used the relation $\Gamma'(z) = \Gamma(z)\psi(z)$ and defined

$$\nu(\alpha) \stackrel{\text{def}}{=} \psi(\alpha + p) - \psi(\alpha).$$

From Lemma 1, it follows that $\nu(\alpha) > 0$ which implies $\mu(\alpha)$ is increasing.

Since $(\cdot)^{1/p}$ is a continuous increasing function, it suffices to show the objective $\mathcal{G} = \mathcal{F}_i^p$ is increasing, given by

$$\mathcal{G}(\alpha_j) = \frac{\mu \left(\sum_{l \neq c} \alpha_l \right) + \sum_{l \neq c} \mu(\alpha_l)}{\mu(\alpha_0)}$$

The derivative is then calculated as:

$$\begin{aligned} \mathcal{G}'(\alpha_j) &= \frac{\mu' \left(\sum_{l \neq c} \alpha_l \right) + \mu'(\alpha_j)}{\mu(\alpha_0)} \\ &- \frac{\mu'(\alpha_0) \cdot \left[\mu \left(\sum_{l \neq c} \alpha_l \right) + \sum_{l \neq c} \mu(\alpha_l) \right]}{\mu(\alpha_0)^2} \end{aligned}$$

The condition $\mathcal{G}'(\alpha_j) > 0$ is equivalent to:

$$\frac{\mu' \left(\sum_{l \neq c} \alpha_l \right) + \mu'(\alpha_j)}{\mu'(\alpha_0)} > \frac{\mu \left(\sum_{l \neq c} \alpha_l \right) + \sum_{l \neq c} \mu(\alpha_l)}{\mu(\alpha_0)} = \mathcal{G}$$

Upon substituting the expression (5), this condition becomes:

$$\begin{aligned} & \mu \left(\sum_{l \neq c} \alpha_l \right) \nu \left(\sum_{l \neq c} \alpha_l \right) + \mu(\alpha_j) \nu(\alpha_j) \\ & > \left[\mu \left(\sum_{l \neq c} \alpha_l \right) + \sum_{l \neq c} \mu(\alpha_l) \right] \nu(\alpha_0) \end{aligned} \quad (6)$$

From Lemma 1, it follows that $\nu \left(\sum_{l \neq c} \alpha_l \right) > \nu(\alpha_0)$ and $\nu(\alpha_j) > \nu(\alpha_0)$. In addition, the functions $\mu \left(\sum_{l \neq c} \alpha_l \right) \nu \left(\sum_{l \neq c} \alpha_l \right)$ and $\mu(\alpha_j) \nu(\alpha_j)$ are both increasing as α_j grows. Using these results and the fact that $\left[\sum_{l \neq c, j} \mu(\alpha_l) \right] \nu(\alpha_0) \rightarrow 0$ as α_j grows (due to Lemma 1), it follows that the inequality (6) holds true for large α_j . Thus, we conclude that the loss function is increasing as α_j gets large. The proof is complete. \square

An illustration of Theorem 2 is shown in Fig. 11 below. An approximate loss function is also shown due to $\lim_{\alpha \rightarrow \infty} \frac{\Gamma(\alpha+p)}{\Gamma(\alpha)\alpha^p} = 1$, from which we obtain the approximation $\mu(\alpha) \sim \alpha^p$. This approximation to the loss behaves similarly. Despite the initial dip, the loss is increasing as α_j increases. We remark that the loss is neither convex nor concave in α_j .

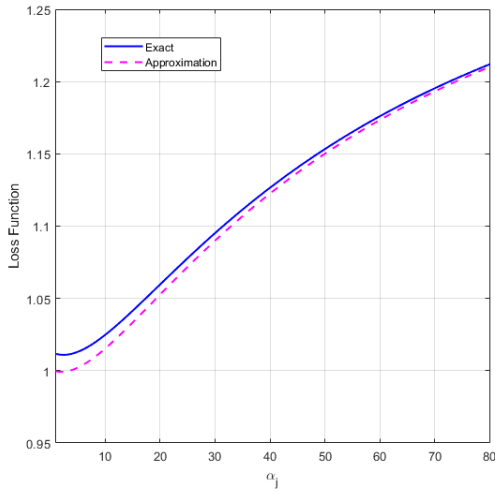


Figure 11: Illustrative example for Theorem 2. Here, the loss function \mathcal{F}_i is plotted as a function of α_j , $j \neq c$. Parameters $p = 2$ and a random α vector were used for $K = 10$ classes with α_c small relative to other concentration parameters. As Theorem 2 shows, the loss is increasing for large α_j .

Proof of Theorem 3

Proof. From Haussler and Opper (1997) (p. 2472), we have

$$\begin{aligned} & \frac{\partial}{\partial \alpha'_i} D_u^R(f_{\alpha} \parallel f_{\alpha'})|_{\alpha'=\alpha} = 0 \\ & \frac{\partial^2}{\partial \alpha'_i \partial \alpha'_j} D_u^R(f_{\alpha} \parallel f_{\alpha'})|_{\alpha'=\alpha} = u J_{ij}(\alpha) \end{aligned}$$

and using Taylor's expansion to second order:

$$D_u^R(f_{\alpha} \parallel f_{\alpha'}) = \frac{u}{2} (\alpha - \alpha')^T J(\alpha) (\alpha - \alpha') + O(\|\alpha - \alpha'\|_2^3) \quad (7)$$

where $J(\alpha)$ is the Fisher information matrix corresponding to the Dirichlet distribution. Taking the logarithm of the density, we have $\log f_{\alpha}(\mathbf{p}) = \log \Gamma(\alpha_0) - \sum_j \log \Gamma(\alpha_j) + \sum_j (\alpha_j - 1) \log p_j$, and differentiating twice we obtain:

$$\begin{aligned} & \frac{\partial}{\partial \alpha_i} \log f_{\alpha}(\mathbf{p}) = \psi(\alpha_0) - \psi(\alpha_i) + \log p_i \\ & \frac{\partial^2}{\partial \alpha_i \partial \alpha_j} \log f_{\alpha}(\mathbf{p}) = \psi^{(1)}(\alpha_0) - \psi^{(1)}(\alpha_i) I_{\{i=j\}} \end{aligned}$$

Since $J_{ij}(\alpha) = -\mathbb{E}[\frac{\partial^2}{\partial \alpha_i \partial \alpha_j} \log f_{\alpha}(\mathbf{p})]$, we obtain:

$$J(\alpha) = \text{diag}(\{\psi^{(1)}(\alpha_i)\}_{i=1}^K) - \psi^{(1)}(\alpha_0) \mathbf{1}_{K \times K}$$

Here $\psi^{(1)}$ is the first order polygamma function. Substituting this into (7) and simplifying, we obtain:

$$\begin{aligned} D_u^R(f_{\alpha} \parallel f_{\alpha'}) & \cong \frac{u}{2} \sum_{i \neq c} \sum_{j \neq c} (\alpha_i - 1)(\alpha_j - 1) J_{ij}(\alpha) \\ & = \frac{u}{2} \left(\sum_{i \neq c} (\alpha_i - 1)^2 \psi^{(1)}(\alpha_i) - \left(\sum_{i \neq c} (\alpha_i - 1) \right)^2 \psi^{(1)}(\alpha_0) \right) \end{aligned}$$

\square

Further MNIST Uncertainty Estimation Results

The uncertainty can also be measured in terms of the inverse Dirichlet strength K/α_0 which captures the spread of the Dirichlet distribution. Fig. 12 shows the resulting performance of various algorithms.

Fig. 13 compares all Dirichlet distribution-based uncertainty estimation methods using the mutual information metric that measures distributional uncertainty on an anomaly detection task.

Fig. 14 compares all Dirichlet distribution-based uncertainty estimation methods using the mutual information metric that measures distributional uncertainty on FGSM adversarial examples detection task. Figs. 15

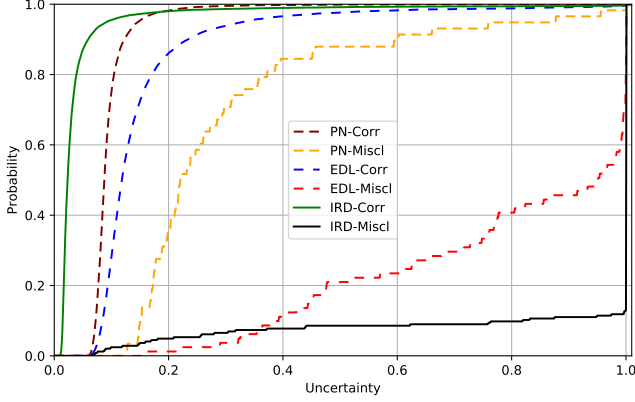


Figure 12: Empirical CDF of inverse Dirichlet strength for correct and incorrect predictions on MNIST dataset.

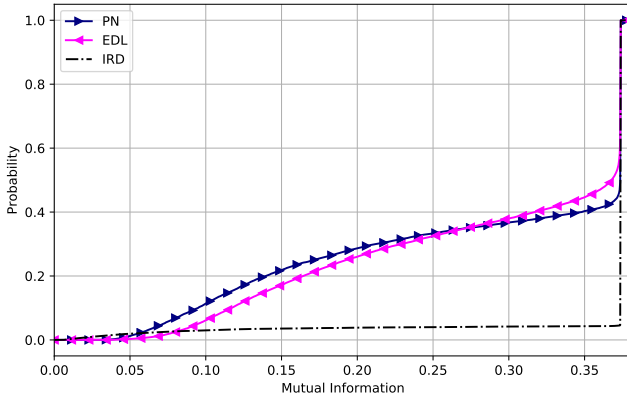


Figure 13: Empirical CDF of mutual information between labels \mathbf{y} and categorical distribution \mathbf{p} out-of-distribution notMNIST dataset.

and 16 show sample digits generated using the FGSM method once the IRD and L2 networks are trained. From left to right, the noise level ϵ is increasing from 0 to 1. We note slightly different things are happening when adversarial noise is added to the images since the adversarial noise is dependent on what features the network has learned to extract and the classification cost function.

Figs. 17 and 18 show sample digits generated using the PGD method once the IRD and L2 networks are trained. From left to right, the noise level ϵ is increasing from 0 to 0.5. We note that the PGD attacks are harder to detect than the simpler one-step FGSM attacks. IRD reliably detects those. Also, we note that the adversarial attacks based on the standard L2 network can be visually detected well for larger enough ϵ , but they are harder to detect for the IRD network, again highlighting the fact that the IRD network has learned different patterns and has a more robust classifier.

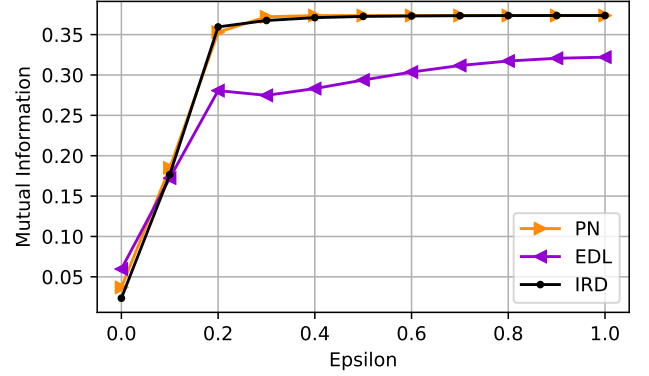


Figure 14: Empirical CDF of mutual information between labels \mathbf{y} and categorical distribution \mathbf{p} out-of-distribution notMNIST dataset.

The adversarial experiment with PGD was repeated for a larger step size of 0.03 with 40 steps to examine trends as larger adversarial steps are taken. Fig. 19 shows the accuracy, predictive entropy and mutual information metrics as the noise level ϵ increases from 0 to 0.5. IRD continues to be the most confident method in terms of detecting these PGD adversarial examples, while PN and EDL lag behind despite the fact that the accuracy of all methods decays as noise increases. Figs. 20 and 21 show sample digits generated using the PGD method once the IRD and L2 networks are trained. From left to right, the noise level ϵ is increasing from 0 to 0.5. We note that the PGD attacks with a larger step size yield more aggressive noise patterns on the digits, still being much more subtle when compared to FGSM. IRD reliably detects those. Furthermore, the adversarial attacks based on the standard L2 network can be visually detected well for larger enough ϵ and shaping of digits into patterns of other digits are apparent, but they are much harder to detect for the IRD network.

Further PhysioNet ECG Uncertainty Estimation Results

Fig. 22 shows the empirical CDF of the inverse Dirichlet strength K/α_0 for various deep learning methods. The IRD method assigns large uncertainty to incorrect predictions, outperforming PN and EDL by a large margin, and low uncertainty to correct ones.

To further test the detection of anomalous signals, we used a subset of the full PhysioNet 17 challenge data labeled as “too noisy to be classified” by experts. A sample of these noisy ECG waveforms is shown in Fig. 23. It is evident that these waveforms are very hard to classify due to transients, low signal to noise ratios and inconsistent temporal statistical behavior. Fig.

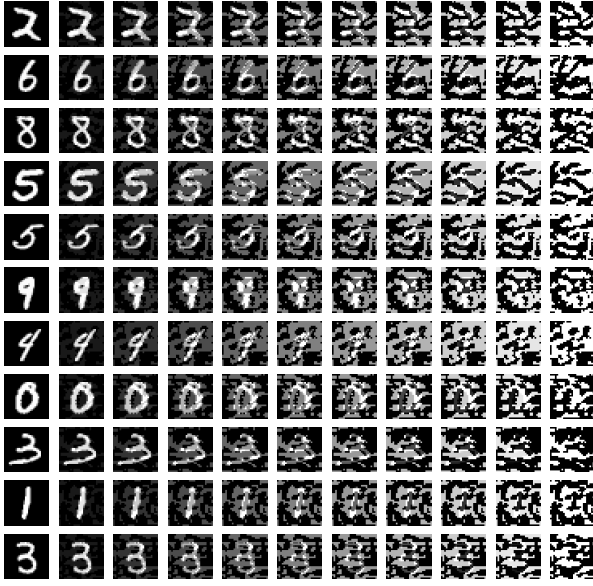


Figure 15: Sample MNIST adversarial digits generated with the FGSM method for the IRD network.

24 shows the empirical CDFs of predictive entropy and mutual information. We observe that IRD assigns higher uncertainty to these noisy ECG recordings than other competing methods implying that the empirical entropy and mutual information distributions are concentrated towards higher values.

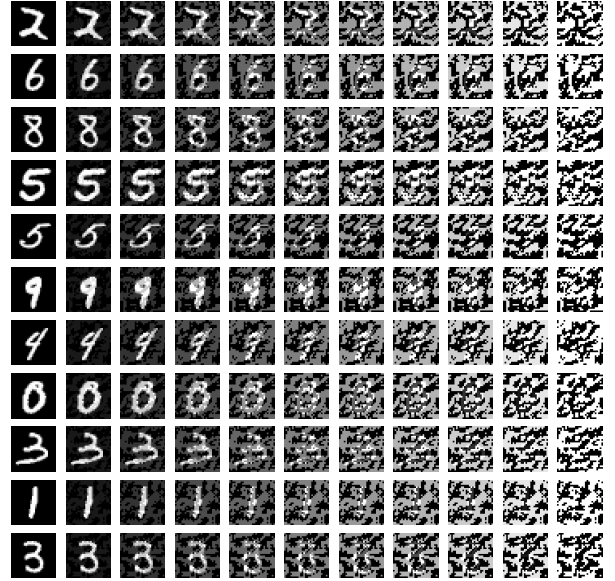


Figure 16: Sample MNIST adversarial digits generated with the FGSM method for L2 network.

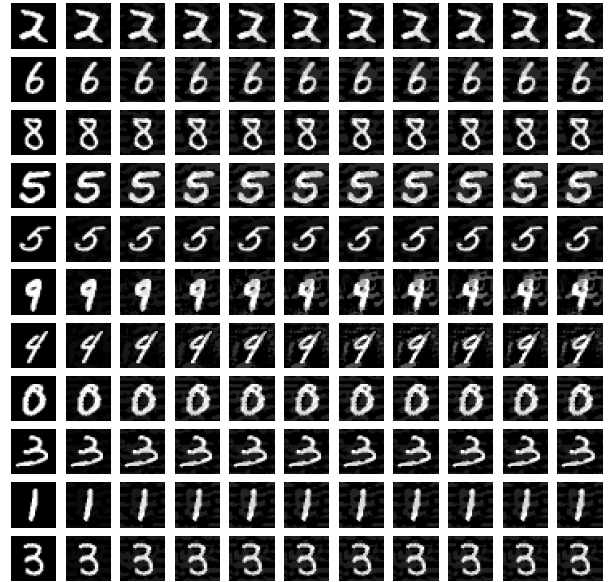


Figure 17: Sample MNIST adversarial digits generated with the PGD method for the IRD network. Here 40 steps were taken with a step size of 0.01.

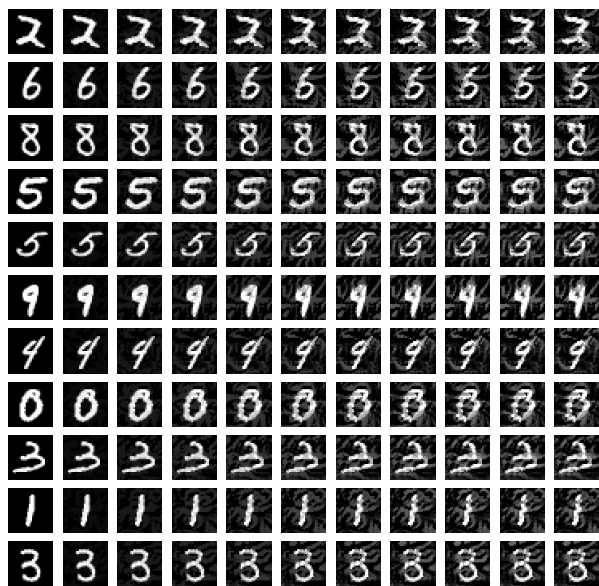


Figure 18: Sample MNIST adversarial digits generated with the PGD method for L2 network. Here 40 steps were taken with a step size of 0.01.

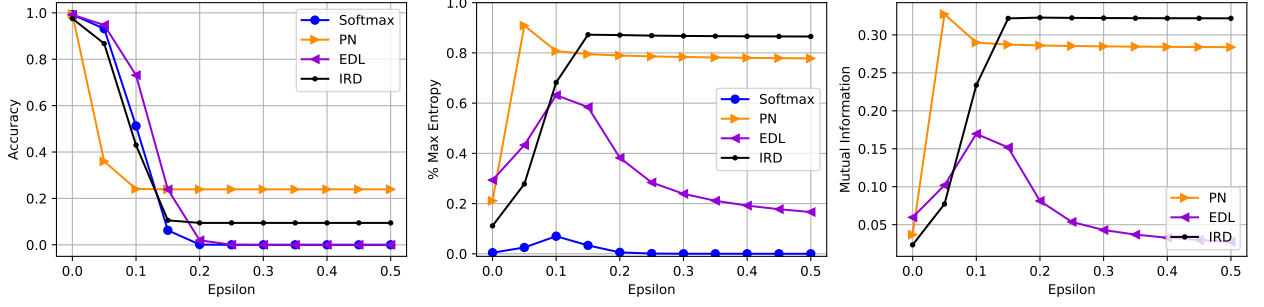


Figure 19: Test accuracy (left), predictive entropy (middle), and mutual information (right) for PGD adversarial examples as a function of adversarial noise ϵ on MNIST dataset. Here, 40 steps were taken with step size 0.03.

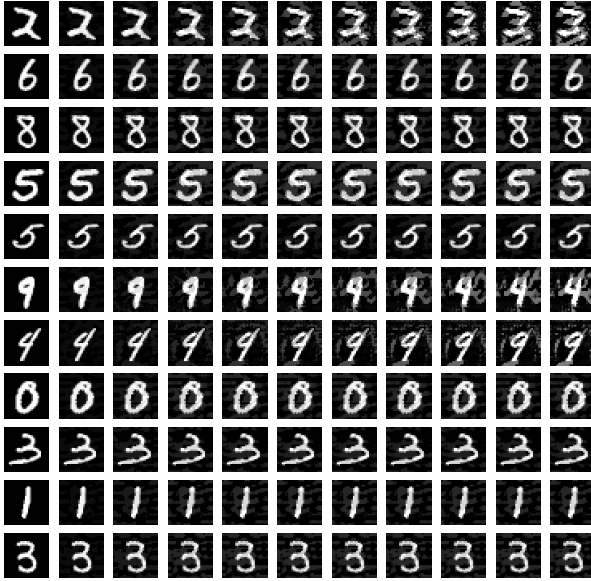


Figure 20: Sample MNIST adversarial digits generated with the PGD method for the IRD network. Here 40 steps were taken with a step size of 0.03.

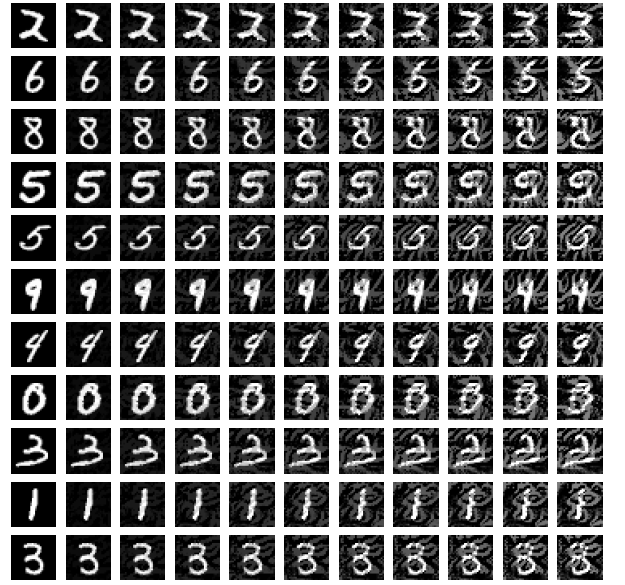


Figure 21: Sample MNIST adversarial digits generated with the PGD method for L2 network. Here 40 steps were taken with a step size of 0.03.

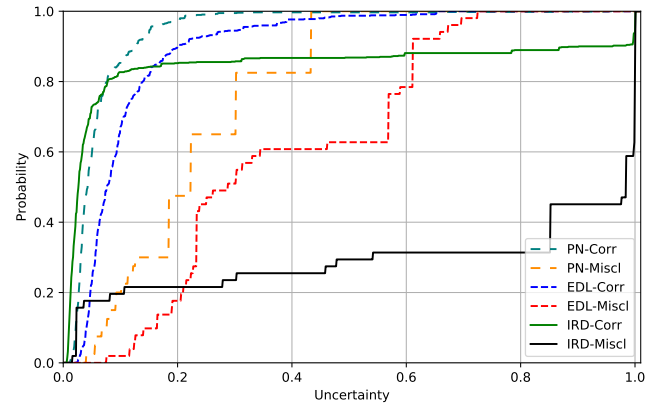


Figure 22: Empirical CDF of inverse Dirichlet strength for correct and incorrect predictions on PhysioNet ECG dataset.

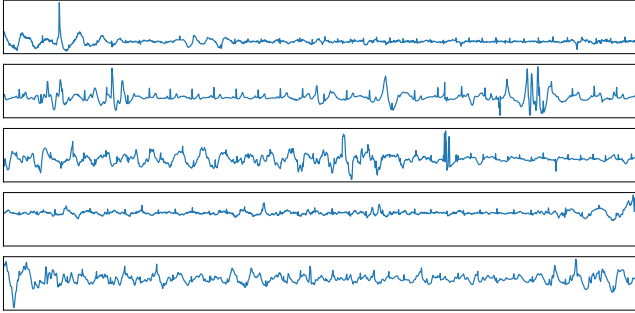


Figure 23: Sample noisy ECG signals from PhysioNet ECG dataset.

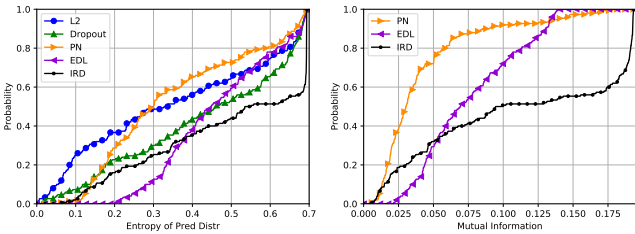


Figure 24: Empirical CDF of predictive entropy and mutual information on noisy ECG signals for various deep learning methods.

References

- Martín Abadi, Paul Barham, Jianmin Chen, Zhifeng Chen, Andy Davis, Jeffrey Dean, Matthieu Devin, Sanjay Ghemawat, Geoffrey Irving, Michael Isard, Manjunath Kudlur, Josh Levenberg, Rajat Monga, Sherry Moore, Derek G. Murray, Benoit Steiner, Paul Tucker, Vijay Vasudevan, Pete Warden, Martin Wicke, Yuan Yu, and Xiaoqiang Zheng. Tensorflow: A system for large-scale machine learning. In *Proceedings of the 12th USENIX Conference on Operating Systems Design and Implementation*, OSDI'16, pages 265–283, Berkeley, CA, USA, 2016. USENIX Association. ISBN 978-1-931971-33-1. URL <http://dl.acm.org/citation.cfm?id=3026877.3026899>.
- B. Alipanahi, A. DeLong, M. T. Weirauch, and B. J. Frey. Predicting the sequence specificities of DNA- and RNA-binding proteins by deep learning. *Nature biotechnology*, 33(8):831–838, 2015.
- C. Blundell, J. Cornebise, K. Kavukcuoglu, and D. Wierstra. Weight Uncertainty in Neural Networks. In *International Conference on Machine Learning (ICML)*, 2015.
- Y. Bulatov. notMNIST dataset, 2011. URL <http://yaroslavvb.com/upload/notMNIST/>.
- T. Chen, E. Fox, and C. Guestrin. Stochastic Gradient Hamiltonian Monte Carlo. In *International Conference on Machine Learning*, 2014.
- D. C. Ciresan, U. Meier, J. Masci, and J. Schmidhuber. Multi-column deep neural network for traffic sign classification. *Neural Networks*, 32:333–338, 2012.
- G. D. Clifford, C. Liu, B. Moody, Li wei H. Lehman, I. Silva, Q. Li, A. E. Johnson, and R. G. Mark. Af Classification from a short single lead ECG recording: the PhysioNet/Computing in Cardiology Challenge 2017. In *Computing in Cardiology*, 2017. URL <https://physionet.org/challenge/2017/>.
- T. Van Erven and P. Harremos. Rényi divergence and Kullback-Leibler divergence. *IEEE Transactions on Information Theory*, 60(7):3797–3820, 2014.
- Y. Gal and Z. Ghahramani. Dropout as a Bayesian Approximation: Representing Model Uncertainty in Deep Learning. In *International Conference on Machine Learning (ICML)*, 2016.
- R. Geirhos, C. R. M. Temme, J. Rauber, M. Bethge, and F. A. Wichmann. Generalization in humans and deep neural networks. In *Advances in Neural Information Processing Systems*, 2018.
- I. J. Goodfellow, J. Shlens, and C. Szegedy. Explaining and Harnessing Adversarial Examples. In *International Conference for Learning Representations*, 2014.
- C. Guo, G. Pleiss, Y. Sun, and K. Q. Weinberger. On Calibration of Modern Neural Networks. In *International Conference on Machine Learning*, 2017.
- D. Haussler and M. Opper. Mutual Information, Metric Entropy and Cumulative Relative Entropy Risk. *The Annals of Statistics*, 25(6):2451–2492, 1997.
- K. He, X. Zhang, S. Ren, and J. Sun. Delving Deep into Rectifiers: Surpassing Human-level Performance on ImageNet classification. In *IEEE International Conference on Computer Vision (ICCV)*, December 2015.
- J. M. Hernandez-Lobato and R. P. Adams. Probabilistic backpropagation for scalable learning of bayesian neural networks. In *International Conference on Machine Learning*, 2015.
- G. Hinton, L. Deng, et al. Deep neural networks for acoustic modeling in speech recognition: The shared views of four research groups. *IEEE Signal Processing Magazine*, 29(6):82–97, 2012.
- N. Houlsby, F. Huszar, Z. Ghahramani, and M. Lengyel. Bayesian Active Learning for Classification and Preference Learning. Technical report, 2011. arXiv:1112.5745.
- D. P. Kingma and J. Ba. Adam: A Method for Stochastic Optimization. In *International Conference for Learning Representations*, 2015.
- D. P. Kingma, T. Salimans, and M. Welling. Variational dropout and the local reparameterization trick. In *Advances in Neural Information Processing (NIPS)*, 2015.
- A. Krizhevsky, I. Sutskever, and G. E. Hinton. ImageNet classification with deep convolutional neural networks. In *Advances in Neural Information Processing Systems (NIPS)*, 2012.
- A. Kurakin, I. J. Goodfellow, and S. Bengio. Adversarial Machine Learning at Scale. In *International Conference for Learning Representations*, 2017.
- B. Lakshminarayanan, A. Pritzel, and C. Blundell. Simple and Scalable Predictive Uncertainty Estimation using Deep Ensembles. In *Advances in Neural Information Processing Systems*, 2017.
- Y. LeCun, C. Cortes, and C.J.C. Burges. The MNIST Database. URL <http://yann.lecun.com/exdb/mnist/index.html>.
- Y. LeCun, Y. Bengio, and G. Hinton. Deep Learning. *Nature*, 521(7533):436–444, 2015.
- K. Lee, H. Lee, K. Lee, and J. Shin. Training Confidence-Calibrated Classifiers for Detecting Out-of-Distribution Samples. In *International Conference for Learning Representations*, 2018.

-
- Y. Li and Y. Gal. Dropout inference in Bayesian neural networks with alpha-divergences. In *International Conference on Machine Learning*, 2017.
- C. Louizos and M. Welling. Multiplicative Normalizing Flows for Variational Bayesian Neural Networks. In *International Conference on Machine Learning (ICML)*, 2017.
- David J.C. MacKay. A practical Bayesian framework for backpropagation networks. *Neural Computation*, 4(3):448–472, 1992.
- A. Madry, A. Makelov, L. Schmidt, D. Tsipras, and A. Vladu. Towards Deep Learning Models Resistant to Adversarial Attacks. In *International Conference for Learning Representations*, 2018.
- A. Malinin and M. Gales. Reverse KL-Divergence Training of Prior Networks: Improved Uncertainty and Adversarial Robustness. Technical report, 2019. arXiv:1905.13472.
- J. G. Mauldon. A generalization of the Beta-distributions. *Annals of Mathematical Statistics*, 30: 502–520, 1959.
- D. Molchanov, A. Ashukha, and D. Vetrov. Variational dropout sparsifies deep neural networks. In *International Conference on Machine Learning (ICML)*, 2017.
- J. E. Mosimann. On the compound multinomial distribution, the multivariate beta-distribution, and correlations among proportions. *Biometrika*, 49:65–82, 1962.
- Alfred Rényi. On measures of entropy and information. In *Fourth Berkeley Symposium on Mathematical Statistics and Probability, Volume 1: Contributions to the Theory of Statistics*, pages 547–561, 1961.
- H. Ritter, A. Botev, and D. Barber. A Scalable Laplace Approximation for Neural Networks. In *International Conference on Learning Representations*, 2018.
- M. Sensoy, L. Kaplan, and M. Kandemir. Evidential Deep Learning to Quantify Classification Uncertainty. In *Advances in Neural Information Processing Systems (NIPS)* 31, 2018.
- S. Sun, C. Chen, and L. Carin. Learning Structured Weight Uncertainty in Bayesian Neural Networks. In *International Conference on Artificial Intelligence and Statistics (AISTATS)*, 2017.
- I. Sutskever, O. Vinyals, and Q. V. Le. Sequence to sequence learning with neural networks. In *Advances in Neural Information Processing Systems*, 2014.
- D. Wang, A. Khosla, R. Gargeya, H. Irshad, and A. H. Beck. Deep Learning for Identifying Metastatic Breast Cancer. Technical report, June 2016. arXiv:1606.05718.
- Y. Wu et al. Google’s neural machine translation system: Bridging the gap between human and machine translation. Technical report, 2016. arXiv:1609.08144.
- W. Xiong, J. Droppo, X. Huang, F. Seide, M. L. Seltzer, A. Stolcke, D. Yu, and G. Zweig. Toward Human Parity in Conversational Speech Recognition. *IEEE Transactions on Audio, Speech, and Language Processing*, 25(12):2410–2423, December 2017.